mater.scichina.com link.springer.com https://doi.org/10.1007/s40843-026-4466-3

Ultrasonic vibration-assisted mechanical coating of Cr powders on 45 steel for superior corrosion resistance

Bangliang Cao[1,2,3], Boyang Wu[1,2,3], Wenzhe Bao[1,2,3], Yu Zhang[1,2,3,4*], Wenqing Ruan[1,2,3], Jie Dong[1,2,3], Chaoqun Pei[1,2,3], Cunhong Yin[5], Dabin Zhang[5], Xiaodi Liu[1,2,3*] and Jiang Ma[1,2,3*]

ABSTRACT **Preparing functional coatings on metallic substrates is an effective approach to anti-corrosion for metallic materials. However, conventional methods are usually time-consuming and highly dependent on heating samples, and thus there are inevitable thermal effects leading to an underdense layer and weak bonding strength, which ultimately causes catastrophic delamination in service. In order to enhance the service reliability and preparation efficiency of coatings, there is a pressing need for an approach that can achieve coating quickly at low temperatures and with strong bonding strength. Herein, we proposed an ultrasonic vibration-assisted mechanical coating (UVAMC) technique and successfully applied it to deposit Cr powders on the 45 steel substrates near room temperature. The uniform and dense Cr coatings with controllable thicknesses (1.85, 13.4, and 23.5 μm) were fabricated within one second under a low processing stress of 31 MPa. The coating had an exceptional interfacial strength of 66.0 MPa, which was attributed to the 10–20 nm zone of interdiffusion at an atomic scale. Simultaneously, the deposited coatings exhibited a corrosion current density close to that of the 304 stainless steel in the 3.5 wt% NaCl solution, indicating excellent corrosion resistance. The compressive and tensile strengths of the deposited samples remain unchanged. In addition, we also deposited Cu, Al, and 316 stainless steel powders and designed the shape of "SZU" on 45 steel through the UVAMC technique. Our results demonstrated that the UVAMC technique is an efficient and flexible way to coat functional powders on metallic materials and enhance specific properties.**

Keywords: ultrasonic vibration, 45 steel, mechanical coating, elemental interdiffusion, corrosion resistance

INTRODUCTION

Corrosion is the deterioration and failure of materials caused by chemical or physical reactions between materials and environmental media [1,2]. It is one of the main causes of the failure of metals, which not only degrades the structural integrity and service life of metallic components, but also causes huge direct and indirect economic losses to society, such as hindering the stable operation of industrial production, and bringing potential safety risks and environmental hazards [3,4]. To alleviate the problem of metal failure induced by corrosion, various strategies have been developed, including alloying [5,6], surface coating [7–9], surface modification [10,11], passivation treatment [12,13], and chemical conversion [14,15]. Among these, surface coating is the most effective and widely used method, as it enhances wear and corrosion resistance while preserving the substrate's bulk mechanical properties.

A variety of processing techniques have been developed for preparing surface coatings, such as thermal spraying [16–18], cold spraying [19,20], electroplating [21–23], vapor deposition [24–26], and laser cladding [27–29]. They have been widely applied in industrial fields with proven technical feasibility, but still exhibit inherent limitations. For instance, thermal spraying and laser cladding rely on high-temperature conditions to fully melt raw powder particles, which inevitably introduces intense heat input and severe thermal shock. These high-temperature processes can cause thermal damage to the substrate, accompanied by significant oxidation and phase transformation within the coating. As a result, both the densification level and corrosion resistance of the coating are degraded. Although cold spraying and electroplating do not require high-temperature conditions, it suffers from a low proportion of metallurgical bonding between particles, poor interfacial adhesion, and low deposition efficiency [30,31]. Electroplating usually employs toxic and harmful solutions containing heavy metals such as chromium, causing severe environmental pollution. Meanwhile, electroplating deposits form weak physical/chemical bonding without metallurgical bonding or elemental interdiffusion, resulting in poor interfacial adhesion, easy delamination, and coating peeling during service [32,33]. In vapor deposition, chemical vapor deposition (CVD) relies on thermal effects to achieve the dissociation of precursors (targets) and the activation of surface chemical reactions, and such high deposition temperatures restrict the selection of substrate materials [34]. On the other hand, coatings synthesized by physical vapor deposition (PVD) generally suffer from high defect density and residual stress [35]. In view of the numerous drawbacks of the above-mentioned traditional coating technologies, there is an urgent need to develop a novel coating approach with low heat input,

[1] State Key Laboratory of Radio Frequency Heterogeneous Integration, Shenzhen University, Shenzhen 518060, China
[2] Shenzhen Key Laboratory of High Performance Nontraditional Manufacturing, Shenzhen University, Shenzhen 518060, China
[3] Guangdong Provincial Key Laboratory of Micro/Nano Optomechatronics Engineering, Shenzhen University, Shenzhen 518060, China
[4] School of Materials Science and Engineering, Wuhan University of Technology, Wuhan 430070, China
[5] College of Mechanical Engineering, Guizhou University, Guiyang 550025, China
* Corresponding author (email: 1910293023@email.szu.edu.cn; xdliu2018@szu.edu.cn; majiang@szu.edu.cn)

© Science China Press 2026

environmental friendliness, and reliable interfacial bonding strength.

Ultrasonic vibration (UV)-assisted machining is an advanced processing technology that exhibits outstanding advantages, especially in enhancing the mobility of surface atoms to promote the bonding of separate materials. Ma *et al.* [36] demonstrated that the stimulation of ultrasound elevates atomic mobility and activity at material surfaces, enabling fast atomic interdiffusion at room temperature without external heating, and even in a liquid environment [37]. In addition to metallic glasses, this method can also be extended to other metallic material systems, such as the forming of metallic glasses and high-entropy alloys [38], or metallic glass/Al-6061 composites with excellent cladding performance [39]. Furthermore, Wu *et al.* [40] demonstrated that ultrasonic vibration activates the atoms on the Cu surface via local plastic deformation and oxide removal, providing adequate kinetic energy for interfacial diffusion and bonding at the Cu/diamond interface. These studies consistently confirm that UV can effectively activate surface atoms and enhance atomic mobility even under low-temperature or room-temperature conditions, without relying on high heat input or melting processes. This unique characteristic endows UV with the capability to facilitate atomic migration and interfacial bonding at low temperatures, thereby enabling reliable metallurgical or interfacial joining between dissimilar materials. Consequently, this characteristic also triggers the present work, which aims to achieve high-strength interfacial bonding by activating atomic activity through UV under low-temperature and low-heat-input conditions. Traditional ultrasonic consolidation and ultrasonic welding only join solid metal sheets for structural assembly and cannot fabricate coatings from powders [41,42]. Differently, ultrasonic vibration-assisted mechanical coating ultrasonic vibration-assisted mechanical coating (UVAMC) uses loose metal powder to form protective coatings on substrates. It only modifies the substrate surface instead of changing bulk matrix properties, and produces both particle bonding inside the coating and metallurgical diffusion interfaces between coating and substrate, which cannot be realized by conventional ultrasonic joining techniques. This process can effectively avoid thermal damage and oxidation caused by high temperature, and promote the interfacial bonding between the coating and the substrate.

In this work, we used UV to deposit Cr powders onto 45 steel, which is termed ultrasonic vibration-assisted mechanical coating. The reason for choosing 45 steel as a substrate is the favorable comprehensive properties and low cost, making it widely used in mechanical manufacturing. However, its compromised corrosion resistance shortens part lifespan in corrosive environments [43]. A dense and uniform Cr coating with variable thickness from 1.85–23.5 μm was deposited on 45 steel by adjusting process parameters, confirming the excellent thickness-tunability of this technology. Though the whole process only takes 1 s at room temperature and low pressure (31 MPa), reliable bonding between the interface of Cr and 45 steel can be achieved. It is confirmed by the exceptional interfacial strength of 66.0 MPa through the scratch adhesion tests, and the high strength benefits from the approximately 10–20 nm-thick elemental interdiffusion transition zone at the atomic scale. Electrochemical tests demonstrate that the sample with Cr coating exhibits a corrosion current density of 0.86 μA cm^{-2} in 3.5 wt% NaCl solution, which is significantly lower than that of bare 45 steel at 76.41 μA cm^{-2} and close to the values of commercial 304 stainless steel (SS) at 0.49 μA cm^{-2} and bulk Cr at 0.42 μA cm^{-2}, indicating excellent corrosion resistance. The compressive and tensile strengths remain almost unchanged, revealing that the UVAMC will not affect the service reliability of 45 steel. Furthermore, the technique demonstrates remarkable process flexibility, not only allowing precise coating of complex patterns "SZU", but also depositing different powders like copper, aluminum, and 316 stainless steel. These findings highlight UVAMC as an efficient strategy for fabricating functional coatings on metallic substrates at room temperature and low pressure, enhancing specific properties that the substrate is insufficient to provide.

EXPERIMENTAL SECTION

Preparation of 45 steel rods and chromium powders

The main component of 45 steel is iron, with trace elements including carbon, chromium, manganese, and nickel. The commercially acquired 45 steel rods with a diameter of 5 mm were used as substrates in this experiment, and the cylindrical disks with a thickness of 3 mm were cut by a low-speed diamond cutting machine (SYJ-150). Additionally, the Cr powders employed in the experiments were commercially obtained high-purity powders with a particle size distribution of 30–70 μm and an elemental purity higher than 99.99 wt%.

Monitoring the applied stress and temperature during UVAMC

An infrared imaging camera (Model 280d, Fotric, China) with a precision of 0.1 K was used to monitor the thermal response on the surface of the 45 steel at a data acquisition frequency of 12 Hz. The samples were placed on a dynamometer (QLMH, QILI, China) to measure the real-time force variations during the UVAMC process. A data acquisition card (National Instruments NI-9237) with a sampling frequency of 1000 Hz was utilized to collect and process the force data, which was subsequently transmitted to a computer via a data acquisition chassis (CDAQ-9174, NI, USA).

Structure characterization of the coated sample

The surface morphology of the samples before and after the coating process and the particle morphology of Cr powders were characterized by a scanning electron microscope (SEM; Quanta FEG 450, FEI, USA). The cross-sectional morphology of the coated samples was also examined to measure the thickness of the Cr coating. The phase structures of the 45 steel, Cr powder, and the coated sample surface were analyzed by an X-ray diffractometer (XRD, Rigaku MiniFlex 600) with Cu-Kα radiation (wavelength: 0.154 nm, rated power: 600 W), with scans performed in a 2θ range from 20° to 90°. The microstructure at the interface was investigated using a transmission electron microscope (TEM; Titan Cubed Themis G2 300, FEI, USA). Energy-dispersive spectroscopy (EDS) attached to the TEM was utilized to analyze the elemental distribution across the interface, and line scanning was conducted to evaluate the variation of elements along specific paths. The particle size distribution of the Cr powder was quantitatively analyzed from the obtained SEM images using ImageJ software.

Simulation method

Molecular dynamics (MD) simulations were performed to

© Science China Press 2026

construct a Fe–Cr bilayer model with a total of 103554 atoms. The system was stacked along the normal direction to form a sharp and flat Fe/Cr interface, in which atoms were arranged in a body-centered cubic (BCC) lattice, and periodic boundary conditions were adopted to eliminate size effects. The interatomic interactions were accurately described by the embedded atom method (EAM) potential tailored for the Fe–Cr system [44]. All simulations were carried out in the isothermal-isobaric ensemble (NPT) at a controlled temperature of 300 K, with a time step of 5 fs and a total simulation duration of 200 ps. After sufficient relaxation, two sets of comparative simulations were conducted: under isothermal conditions at 300 K, atomic diffusion was driven solely by thermal activation; a 3% strain was applied to equivalently mimic the mechanical shock induced by ultrasonic energy. The actual UVAMC experiment adopts a sinusoidal ultrasonic vibration with an amplitude of 44 μm. However, obvious mismatches exist between the macro experimental scale and picosecond MD simulation scale in both time and space, so a strict one-to-one numerical conversion between the actual vibration amplitude and simulated strain cannot be realized. The strain-time curve of the MD model presents a triangular wave with a single vibration period of 25 ps. To quantify the dynamic loading intensity of ultrasonic impact, the strain rate is calculated via the formula: $\dot{\varepsilon}_{max} = 2\pi f \cdot \varepsilon_{peak}$, where f is the vibration frequency and ε_{peak} denotes the peak strain. According to Fig. S3, the theoretical sinusoidal peak strain rate is calculated as 7.54×10^{9} s^{-1}, while the actual strain rate obtained from the slope of the triangular strain waveform is 2.4×10^{9} s^{-1}. The two values are at the same order of magnitude. It reflects the ultrahigh dynamic loading feature of ultrasonic treatment. The interfacial atomic configurations and the mean squared displacement (MSD) data were extracted from the simulation trajectories, and the MSD was used to quantitatively characterize atomic migration ability. The formula is expressed as $\mathrm{MSD} = \frac{1}{N}\sum_{i=1}^{N}|r_i(t) - r_i(0)|^2$, where $r_i(t)$ and $r_i(0)$ represent the position of atom i at time t and the initial position, respectively, and N is the total number of atoms counted. This approach was adopted to reveal the regulation mechanism of UV on the diffusion behavior of the Fe–Cr interface.

Characterization of mechanical properties

The surface hardness of both the as-received sample and the Cr-coated sample after UVAMC was measured by an automatic Vickers hardness tester (HM-210, MITUTOYO, Japan). The tests were performed under a load of 500 gf (4.90 N) for 10 s. Ten measurement points were uniformly selected within a 2 mm×2 mm area to take an average. To characterize the hardness and modulus of the diffusion region between the Cr coating and the substrate, nanoindentation experiments were conducted using a Berkovich tip with a radius of 20 nm. A scratch test was performed on the coated sample surface using a testing system (TI 980, Bruker, Germany) equipped with a Berkovich tip to evaluate the interfacial adhesion strength between the Cr coating and the 45 steel substrate. The quasi-static compressive and tensile tests were conducted by a universal testing machine (UTMS305H, SANSI, China). The experiments were performed under ambient conditions. The specimens for the compressive test had dimensions of 5 mm in diameter and 10 mm in height, with a strain rate of 8.33×10^{-4} s^{-1}, while the tensile test specimens measured 20 mm in length, 8 mm in width, and 2 mm in thickness, with a strain rate of 1.03×10^{-4} s^{-1}.

Corrosion resistance tests

Electrochemical measurements were conducted by a CHI660e electrochemical workstation (Chenhua, China). All tests were carried out in a three-electrode system; the sample served as the working electrode, an Ag/AgCl electrode as the reference electrode, and a platinum sheet as the counter electrode. Before testing, all samples were ultrasonically cleaned in ethanol and then dried in air. The 3.5 wt% NaCl solution was used as the electrolyte. During the measurement, the open-circuit potential (OCP) was monitored for 1800 s. Subsequently, electrochemical impedance spectroscopy (EIS) and potentiodynamic polarization measurements were conducted. EIS tests were performed over a frequency range from 100 to 0.01 Hz with an amplitude of 5 mV. The polarization curves were scanned from −1.6 to 1.2 V at a scan rate of 1 mV s^{-1}. The EIS data were fitted using ZView software, and the polarization curves were analyzed by the Tafel extrapolation method. All electrochemical tests were repeated at least three times to ensure repeatability.

Ultrasonic vibration setup

The UV device used in this experiment is illustrated in Fig. 1a, which consists of six main components: a pneumatic system, a control system, a power supply, a transducer, a booster, and a horn. The power supply generates high-frequency electrical energy, which is then transmitted to the transducer. The electrical energy is converted into mechanical vibrations through the piezoelectric materials inside the transducer. The booster amplifies the amplitude of the mechanical vibrations up to 44 μm, and the horn transfers the amplified vibrations to the surface of the 45 steel, causing the Cr powders on the surface to fracture and form a metallurgical bond with the substrate. The force between the sample and the horn is provided by the pneumatic system, where high-pressure gas stored in the air pump is converted into mechanical pressure through a pneumatic piston. In addition to the mechanical hardware unit, a control system precisely regulates the applied pressure, ultrasonic amplitude, and ultrasonic energy.

RESULTS AND DISCUSSION

Display of coated samples

Fig. 1b demonstrates a photo of as-received 45 steel before and after UVAMC treatment, the coated sample showing a uniform and dense Cr film completely covering the surface of the substrate. The morphology of raw Cr powders is shown in Fig. 1c. The as-received Cr particles exhibit irregular polyhedral structures with particle sizes mainly distributed in the range of (60±15) μm. Fig. 1d shows a comparative XRD analysis that reflects the structural evolution caused by coating. The 45 steel displays characteristic α-Fe diffraction peaks corresponding to the (110), (200), and (211) planes. The Cr-coated sample exhibits distinct diffraction peaks at 2θ positions that match the (110), (200), and (211) crystal planes of Cr, confirming the formation of a crystalline Cr phase in the coating. Notably, the relative intensities of these peaks differ from those of the particulate Cr reference, suggesting the presence of a preferred orientation induced by the coating process. This texture evolution is likely

© Science China Press 2026

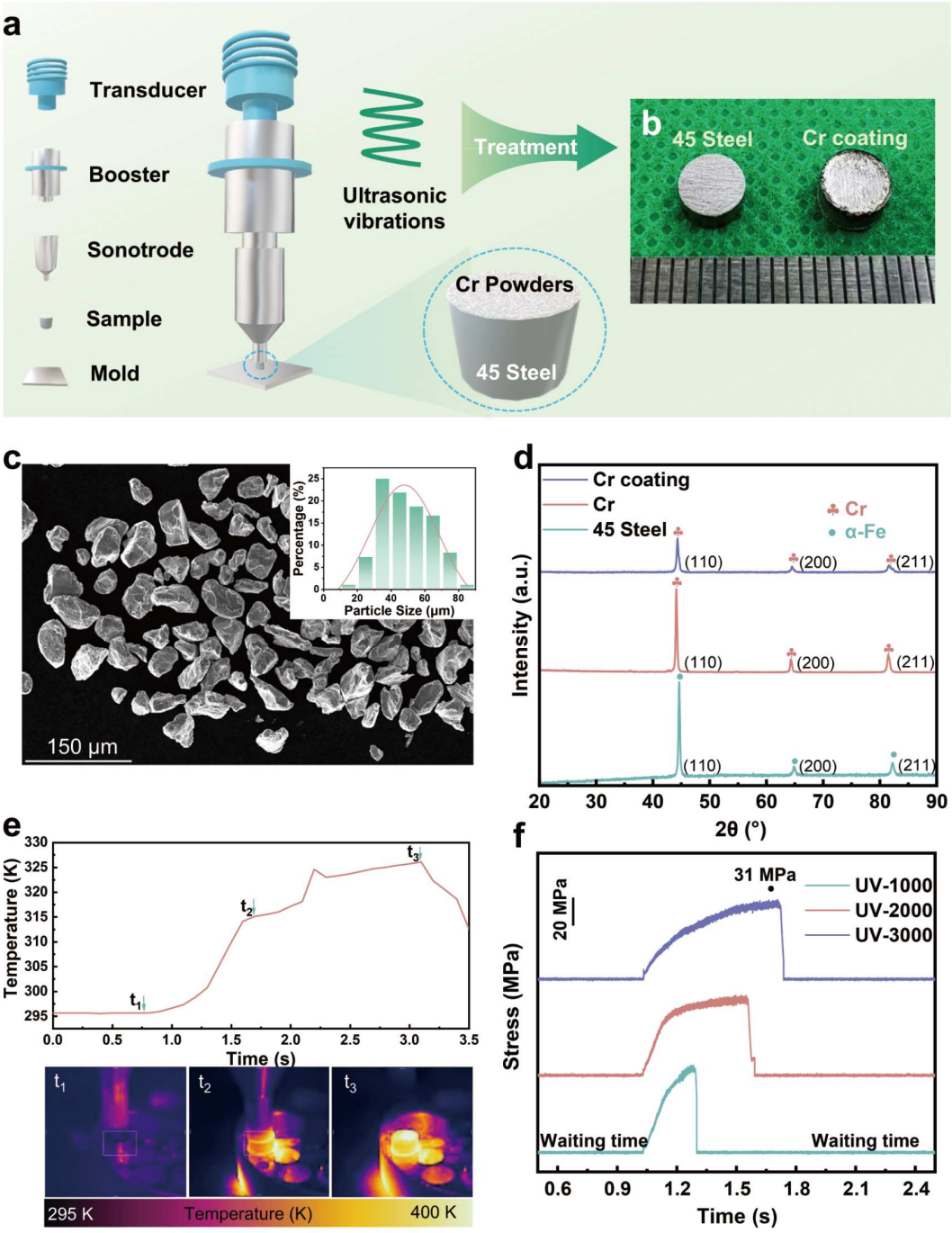

Figure 1 (a) Schematic illustration of the UVAMC and UV setup. (b) Photo of as-received 45 steel sample and Cr-coated sample. (c) SEM images of Cr powders, with the inset showing their particle size distribution. (d) XRD patterns of Cr powders, 45 steel, and the deposited Cr coating. (e) Surface temperature curve and captured infrared thermal images during sample preparation under 3000 J UV energy. (f) Variation of applied stress during UV under 1000, 2000, and 3000 J energy levels.

attributed to the directional impact of particles and subsequent plastic deformation during deposition, consistent with the typical behavior observed in metallic coatings [45,46]. Further analysis reveals a slight broadening of the diffraction peaks in the coated Cr compared to its particulate counterpart. Using Scherrer's equation ($D=K\lambda/\beta\cos\theta$, with K=0.94 and λ= 0.15406 nm, where K is the shape factor and λ represents the X-ray wavelength) [47], the average crystallite size of the Cr coating is estimated to be approximately 23 nm, which is significantly smaller than the raw Cr powder (≈85 nm). This grain refinement can be attributed to dynamic recrystallization induced by high-frequency UV during the UVAMC process, which promotes grain fragmentation and suppresses grain growth [48]. Additionally, a minor shift of the diffraction peaks toward higher 2θ angles (≈0.2°) is observed on the curve of the Cr coating, indicating the presence of residual compressive stresses, which is likely a result of the rapid plastic deformation and the constrained cooling of the deposited particles. Collec-

© Science China Press 2026

tively, the XRD results demonstrate that UVAMC enables the formation of a nanostructured, stress-modified Cr coating with high phase purity, which underpins its exceptional mechanical properties and corrosion resistance.

The infrared image in Fig. 1e demonstrates the temperature variation during the UVAMC process with 3000 J. Before the process begins, it remains stable at approximately 295 K (room temperature) until time t_1, when the vibrations begin; the temperature rises gradually and peaks at 325 K. Due to the process temperature being significantly lower than the recrystallization temperature of the Cr particles, the thermal effects of instantaneous temperature rise can be ignored, and the process can be considered to be conducted at near room temperature. Fig. 1f presents the investigation of the process stress of UVAMC process characteristics under different energy inputs (1000, 2000, 3000 J). The curve consists of two parts, which are the waiting time and the processing time. During the waiting time, the stress remains unchanged without fluctuations, increases when the horn contacts the surface of 45 steel covered with Cr powders, and starts to vibrate. Although the applied stress is positively correlated with the increase in process energy, the maximum stress to deposit Cr powders at 3000 J energy is only 31 MPa. These results demonstrate that the UVAMC technology combines both high efficiency and low energy consumption.

Structural characterization of coated samples

Fig. 2a presents a comparison of surface morphologies before and after UVAMC, demonstrating that the Cr coating exhibits outstanding surface continuity and densification. Cross-sectional characterization (Fig. 2b) ensures the formation of a typical lamellar structure with an average thickness of 13.4 μm under the energy input of 2000 J, showing reliable bonding with

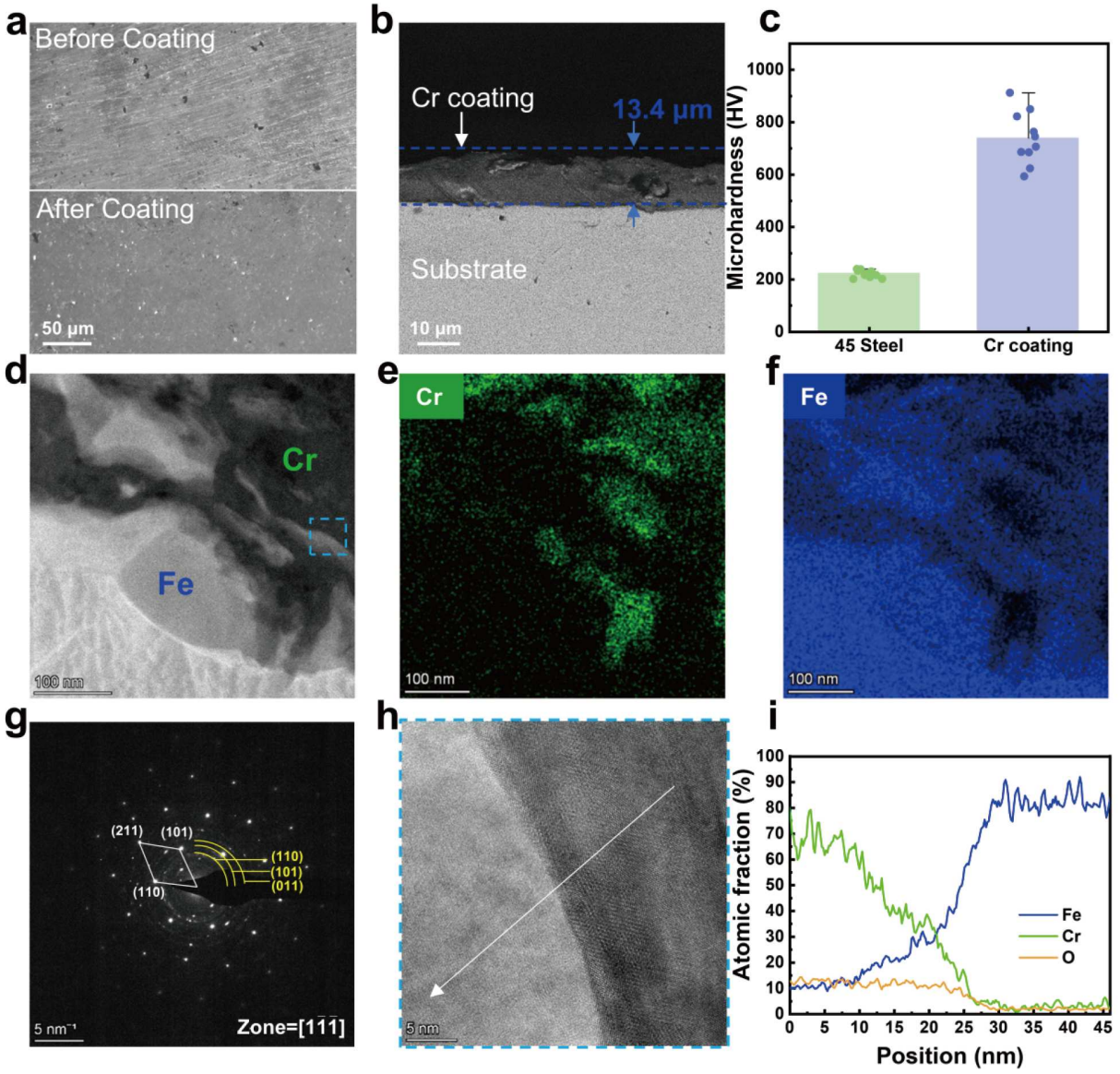

Figure 2 (a) SEM morphology of the sample surface before and after UVAMC. (b) SEM image of the Cr coating. (c) Vickers hardness of the 45 steel and Cr-coated sample surfaces. (d) TEM image of the interface between Cr and Fe elements. EDS map of the (e) Cr and (f) Fe element. (g) SAED obtained from the region indicated in (d). (h) High-resolution transmission electron microscopy (HR-TEM) image of the interface between Cr and Fe. (i) Line scan profiles of Cr, O, and Fe elements along the white arrow in (h).

© Science China Press 2026

the substrate without observable microcracks or voids at the interface. Moreover, the thickness of coatings can be tuned by adjusting the input energy. As shown in Fig. S1, the coating thickness is only 1.85 μm at 1000 J, and it reaches 23.5 μm at 3000 J. Furthermore, three repeated tests were carried out for each set of energy parameters (Fig. S1d), the average coating thicknesses under different energies are 1.74, 14.15, and 22.35 μm, and the small data fluctuation verifies the reliable repeatability and stable controllability of the coating preparation process. Microhardness tests (Fig. 2c) show the Cr coating has an average hardness of 700 HV, 3.5 times higher than the 200 HV substrate. This improvement mainly stems from the inherent hardness of Cr, grain refinement, and UV-induced work hardening. To verify the interfacial bonding quality between the coating and the substrate, systematic nanoindentation characterization was conducted on the cross-sectional coating-substrate interfacial region. As shown in Fig. S2, the hardness and elastic modulus peak at 5 μm from the coating surface, with the average values of 8.44 and 258.75 GPa, respectively, indicating a dense and high-performance Cr layer. With the test position moving toward the substrate to 10 and 15 μm, the hardness and modulus decrease gradually, which can be ascribed to the interdiffusion of Cr and Fe under UV and the *in-situ* formation of new phases such as intermetallic compounds or solid solutions. At a position of 20 μm from the coating surface, the mechanical properties reach the minimum, corresponding to the original 45 steel substrate. The continuous gradient distribution of mechanical properties confirms the formation of a defect-free and robust diffusion interface between coating and substrate. The high-resolution interfacial analysis (Fig. 2d–f) further elucidates the metallurgical bonding characteristics: a well-defined transition zone formed by mutual diffusion of Fe and Cr elements, along with defect-free interfacial bonding. Fig. 2h displays a high-resolution morphology of the interfacial region within the blue dashed area in Fig. 2d, revealing a high-quality direct bonding between Cr and Fe at the atomic scale with a continuous interface free from cracks or pores. Combined with the line-scanning profile across the interface in Fig. 2i, an interdiffusion layer with a width of approximately 10–20 nm can be observed, indicating mutual mixing of Cr and Fe at the interface and achieving robust embedding of Cr within the Fe matrix. This optimized interfacial architecture endows the coating system with superior bonding strength and exceptional spallation resistance. To confirm the direct bonding of Cr and Fe, Fig. 2g shows the selected-area electron diffraction (SAED) pattern corresponding to the dashed blue box region in Fig. 2d. It consists of a set of diffraction spots. By analyzing these spots, we can identify that the diffraction spots match well with the crystal planes of the Cr-rich phase. For example, the spots corresponding to the (110), (211), and other crystal planes can be clearly indexed, indicating the crystalline nature of the Cr-rich phase at the interface.

Coating deposition mechanism

Fig. 3 illustrates the dynamic formation process of the Cr coating on 45 steel under UV, depicted through schematic diagrams (Fig. 3a–h) and corresponding microstructural/SEM images (Fig. 3i–k). Fig. 3l, m presents atomic configurations and MSD curves from MD simulations that reveal the interfacial diffusion behavior of Cr–Fe under UV. Specifically, the schematic in Fig. 3a–d outlines the core stages of coating evolution, while the cross-sectional views (Fig. 3e–h) and SEM images (Fig. 3i–k) provide direct evidence of microstructural evolution, from powder accumulation to final densification.

At 0 s (Fig. 3a, e), Cr powders are loosely placed on the 45 steel surface, with a pre-existing oxide layer acting as a barrier at the interface. After 0.4 s of vibration (Fig. 3b, f, i), under cyclic stress, the Cr powders undergo crushing and plastic deformation, achieving preliminary interlocking bonding. However, inter-particle voids and cracks still exist, proved by the porous structure and mechanical interlocking in the microstructure. From 0.4 to 0.8 s (Fig. 3c, g, j), continuous vibration drives crack healing. The intense local stress generated by UV further ruptures the oxide layer at the interface, exposing fresh and reactive metal surfaces. This rupture eliminates the diffusion barrier, enabling rapid atomic diffusion and rearrangement between the Cr coating and the 45 steel substrate. The resulting interdiffusion layer acts as a "metallurgical bridge", promoting crack closure and pore filling while significantly improving interfacial adhesion, even under low-temperature conditions (Fig. 3c, g, j). To 1.0 s (Fig. 3d, h, k), a dense Cr coating is formed on the 45 steel surface. The microstructure shows uniformly dispersed oxide particles within the coating matrix, and the SEM image reveals a compact structure free of visible cracks or porosity. This final densification is attributed to the synergistic effects of severe plastic deformation and sustained atomic diffusion driven by UV [49]. The high strain-rate deformation refines the grain structure, while the ongoing atomic diffusion homogenizes the element distribution, consolidating the coating into a single, integral layer with strong interfacial bonding.

Notably, despite the high hardness of Cr, extremely high strain-rate deformation and localized stress concentration under UV activate interface reactions and atomic diffusion, which are critical for the formation of the void-free, dense microstructure. The MD simulation results (Fig. 3m) further verify this mechanism: under isothermal conditions at 300 K, the Cr–Fe interface maintains a clear layered structure throughout the 200 ps simulation, with only a negligible number of atoms crossing the initial interface; MSD data show only gradual, limited increases in Fe and Cr displacements, indicating that low heat cannot overcome the interfacial diffusion barrier, thereby restricting atomic mobility and interdiffusion. In contrast, under the ultrasonic impact with the energy of 3000 J, the interface rapidly blurs over time, with the Fe and Cr atoms significantly penetrating each other's lattices to form a continuous transition layer; the MSD curves (Fig. 3l) exhibit a steep upward trend, with the Fe and Cr MSD values reaching approximately 0.75 and 0.68 $Å^2$ at 200 ps, which are 1.8 and 2.3 times those of the 300 K isothermal group at the same time scale.

Collectively, these results confirm that high-energy mechanical impact from UV can convert mechanical energy into atomic kinetic energy and accelerate interfacial atomic migration, which acts as the core driving force for intensive Fe–Cr interdiffusion. In this process, powder fragmentation, plastic deformation, and mechanical interlocking first eliminate surface oxide barriers to form temporary physical bonding; the subsequent ultrasonic-induced element interdiffusion generates a continuous ~10–20 nm metallurgical transition layer and dominates the reliable interfacial adhesion. Overall, UVAMC densifies the Cr coating and strengthens interfacial bonding even with native initial oxidation layers.

© Science China Press 2026

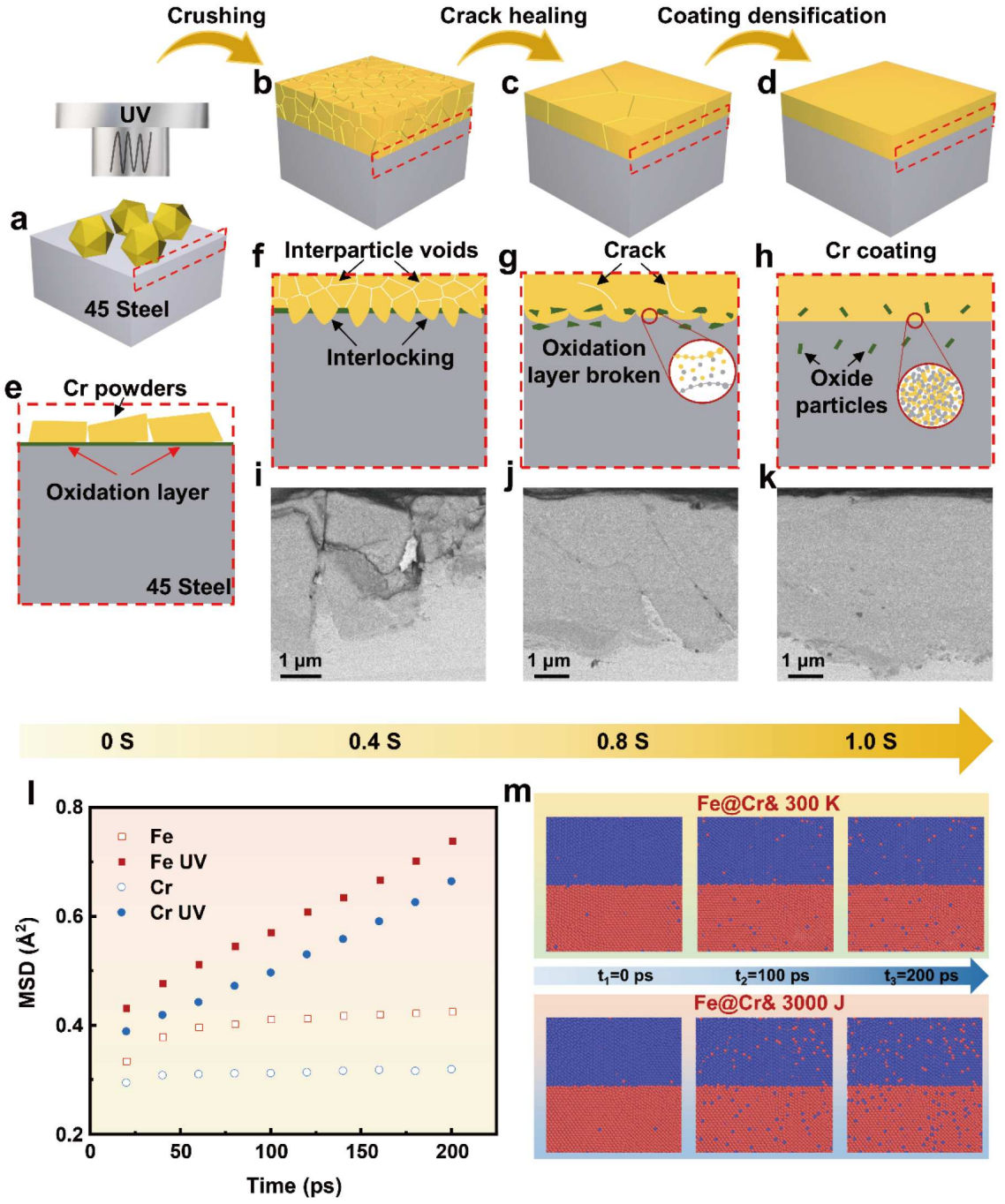

Figure 3 Schematic illustration of the UVAMC Cr coating formation process. (a) Initial state of Cr powder particles on the 45 steel substrate (macro). (b) The Cr powders are crushed and fill the surface of 45 steel (macro). (c) Healing of defects within the Cr coating (macro). (d) UV facilitates the densification of the Cr coating (macro). (e) The presence of an oxidation layer at the interface between Cr powders and 45 steel corresponding to the microstructure of (a). (f) Plastic deformation and mechanical interlocking of particles corresponding to the microstructure of (b) after 0.4 s of UV. (g) Crack healing and oxidation layer broken corresponding to the microstructure of (c) after 0.8 s of UV. (h) Fully dense and continuous Cr coating corresponding to the microstructure of (d) after 1.0 s of UV. (i) SEM image of the microstructure at the initial state (0.4 s). (j) SEM image of the microstructure at the 0.8 s stage. (k) SEM image of the microstructure at the 1.0 s stage. (l) Mean squared displacement curves from MD simulations at 300 K, with and without an applied strain of 3%. (m) Atomic configurations from molecular dynamics simulations: blue and red spheres represent Cr and Fe atoms.

Electrochemical corrosion behaviors

Fig. 4a presents the open-circuit potential evolution of various samples in 3.5 wt% NaCl solution, monitored over 1800 s to evaluate their corrosion thermodynamic stability [50,51]. In 3.5 wt% NaCl solution, all samples displayed thermodynamic characteristics of tending toward a stable surface state. The bulk Cr sample exhibited a relatively positive initial potential with a slight positive shift over time, reaching approximately −0.22 V after 1800 s. Similarly, 304 stainless steel showed a gradual positive shift in potential and arrived at about −0.26 V after 1800 s. The Cr coating exhibited an overall stable potential of −0.42 to −0.46 V, with a slight negative drift likely attributed to

© Science China Press 2026

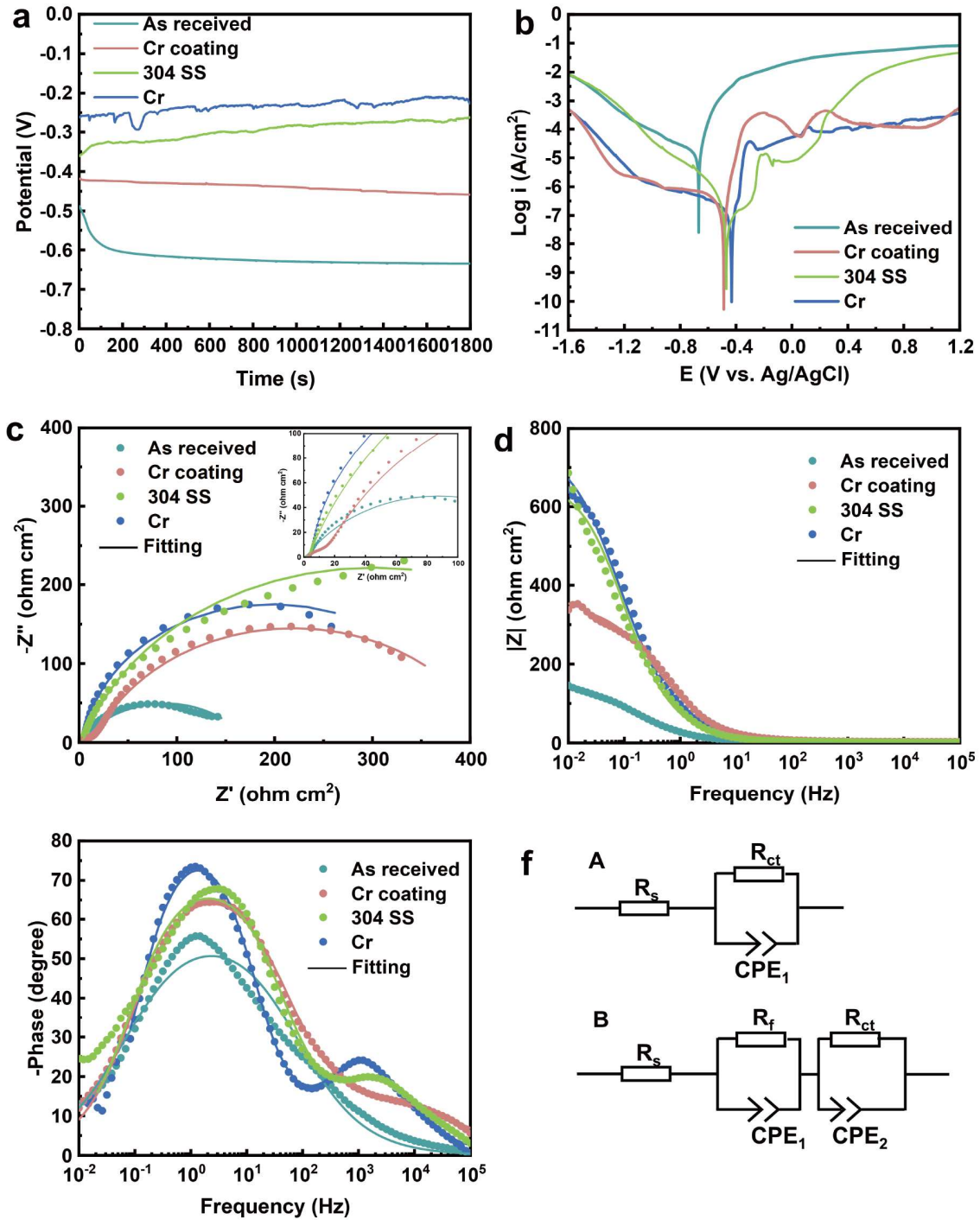

Figure 4 (a) Open circuit potential curves of samples in 3.5 wt% NaCl solution. (b) Potentiodynamic polarization curves of the samples. (c) Nyquist curves of the samples. The inset presents an enlarged view of their high-frequency region. (d, e) Bode curves of the samples. (f) Corrosion equivalent circuit model of the samples. (A) 45 steel, (B) Cr coating, 304 SS, bulk Cr.

slow corrosion at coating micro-defects or elevated surface roughness. The as-received 45 steel possessed the most negative initial potential (approximately −0.5 V) and exhibited a rapid negative shift to −0.63 V within 200 s before stabilizing, indicating a more active thermodynamic tendency toward corrosion.

Fig. 4b shows the potentiodynamic polarization curves of different specimens in 3.5 wt% NaCl solution, and the corresponding electrochemical parameters are listed in Table S1. The corrosion current density (I_{corr}) and potential (E_{corr}) were determined using Tafel extrapolation. Both the Cr coating and the bulk Cr exhibit obvious passivation behavior, indicating that the Cr coating has high density, similar to that of the bulk Cr, and retains the typical passive film formation ability. The E_{corr} of the Cr coating is −0.485 V, which is higher than −0.688 V for the 45 steel but slightly lower than −0.423 V for bulk Cr and −0.443 V for 304 stainless steel. It suggests that the Cr coating

© Science China Press 2026

can act as a continuous and dense physical barrier, effectively isolating the 45 steel substrate from the NaCl solution and thus providing significant corrosion protection. Meanwhile, the slightly lower E_{corr} relative to bulk Cr and 304 stainless steel reflects that the coating still contains a small number of micro-defects or internal stress, leading to slightly lower thermodynamic stability than bulk Cr and 304 stainless steel. The I_{corr} of the Cr coating is 0.86 μA cm^{-2}, which is much lower than 76.41 μA cm^{-2} for the 45 steel and close to 0.49 μA cm^{-2} for 304 stainless steel and 0.42 μA cm^{-2} for bulk Cr. Such low I_{corr} indicates that its corrosion resistance is superior to that of the substrate and even comparable to stainless steel; it also reflects fewer internal defects and good interfacial bonding in the coating, making it difficult for chloride to penetrate and diffuse along defects inside the coating and at the coating-substrate interface.

The corrosion behavior of the samples in 3.5 wt% NaCl solution was characterized by successive electrochemical impedance spectroscopy. Fig. 4c presents the Nyquist plots of all samples. Generally, a larger capacitive arc in the Nyquist plot corresponds to higher charge-transfer resistance (R_{ct}), more pronounced kinetic suppression of corrosion, and superior corrosion resistance. The Cr coating, bulk Cr, and 304 stainless steel all exhibit high-frequency capacitive arcs associated with charge-transfer processes at the metal/passive film interface, indicating that the UV-deposited Cr coating forms a stable passive film. For passivation systems, the low-frequency capacitive arc reflects ion transport inside the passive film, and a larger radius indicates higher compactness and fewer defects of the passive film. For active dissolution systems without a passive film, the low-frequency capacitive arc corresponds to the charge-transfer process at the electrode/electrolyte interface, whose radius represents the charge-transfer resistance, and a larger radius corresponds to better corrosion resistance. The comparison of the low-frequency capacitive arc radii shows that the semicircle radius of the Cr coating is significantly larger than that of the 45 steel and close to bulk Cr and 304 stainless steel. It demonstrates that the Cr coating exhibits better corrosion resistance than the 45 steel substrate, forms a stable passive film in corrosive media, and presents interfacial impedance characteristics basically consistent with typical passivation systems such as bulk Cr and 304 stainless steel.

Fig. 4d, e presents the Bode plots of all samples. The impedance modulus at 0.01 Hz reflects the total resistance of the passive film or coating [52], interfacial charge-transfer resistance, and mass transport resistance, and it is often used as a semi-quantitative indicator to evaluate the corrosion resistance of materials [53]. The impedance modulus of the Cr coating at 0.01 Hz is higher than that of 45 steel, but lower than bulk Cr and 304 stainless steel. Although the Cr coating has formed a continuous and dense passive film that blocks corrosive media and improves the corrosion resistance, the coating still contains a small number of microcracks, allowing the aggressive electrolyte to diffuse through them and eventually reach the 45 steel. The stability of the passive film can be reflected in the mid-frequency region. It can be observed from the Bode phase angle plots that the passive film stability of the Cr coating is close to that of 304 stainless steel and bulk Cr. This improvement is possibly attributed to UV, it may refine grains, homogenize element distribution, and diminish coating defects to help form a more protective Cr passive film [54,55].

The electrochemical characteristics of the Cr coating, 304 stainless steel, bulk Cr, and 45 steel in 3.5 wt% NaCl solution were quantitatively analyzed using equivalent circuit models, and the fitting parameters are listed in Table S2. Model A and Model B in Fig. 4f correspond to the corrosion processes of 45 steel, Cr coating, 304 stainless steel, and bulk Cr, respectively. R_s, R_f, and R_{ct} represent the solution resistance, passive film resistance, and charge-transfer resistance; CPE_1 and CPE_2 denote the passive film capacitance and interfacial capacitance. The passive film thickness is generally negatively correlated with CPE_1: a smaller CPE_1 value indicates a thicker passive film [53,56]. Comparison of the data in Table S2 shows the CPE_1 value of the Cr coating is slightly larger than bulk Cr and 304 stainless steel, suggesting a relatively thinner passive film. The R_f of the Cr coating is higher than the R_{ct} of the 45 steel, indicating that the ion transport resistance within the passive film is larger than that on the 45 steel surface, and the coating exhibits favorable corrosion resistance.

Interfacial bonding strength and mechanical tests of samples

The interfacial bonding strength between the coating and substrate is a critical determinant of corrosion resistance. Interfacial failure facilitates wedge-shaped penetration of corrosive media along the interface, accelerating coating delamination and substrate corrosion. In this study, a synergistic analytical framework combining friction evolution, mechanical response, and multi-scale characterization was constructed via scratch testing, aiming to provide mechanistic insights into the failure behavior of the coating. As illustrated in Fig. 5a, the friction behavior of the deposited coating (red curve) exhibits three distinct stages: during the 0–300 μm stage, the coefficient of friction (COF) remains stable at a low level (<0.5), indicating an intact coating that provides effective wear-resistant barrier protection. Between 300 and 450 μm, the COF increases continuously from 0.5 to 1.25, corresponding to progressive penetration of the probe through the coating, characterized by localized damage without full penetration; this rise in friction is attributed to surface roughening at damage sites and non-uniform contact between the coating and probe. Beyond 450 μm, the COF drops abruptly to the values of the 45 steel substrate (yellow curve), signifying complete coating failure and direct probe-substrate contact. Complementary SEM morphology and EDS compositional analyses further corroborate: within the 300–450 μm interval, the scratch depth progressively increases while the coating-specific element (e.g., Cr) remains dominant despite a decreasing concentration, confirming the progressive damage phase of the coating. At the critical 450 μm position, the scratch morphology exhibits significant deepening and widening, accompanied by a sharp rise in the substrate-specific element (Fe) concentration, marking the complete coating spallation and substrate exposure. The COF variation matches well with the morphological and elemental evolution, confirming 450 μm as the critical failure displacement of the coating.

From Fig. 5b, it can be determined that the normal force is 0.363 N at the coating failure position of 450 μm. Based on the Hertzian contact theory [57], combining the elastic modulus, Poisson's ratio, the probe radius (r=5 μm), and the bonding force (F_a=0.363 N), the interfacial bonding strength was calculated to be 66.0 MPa using the following Equation (1). This peak represents the critical interfacial bonding strength threshold. Exceeding this value triggers the transition from localized

© Science China Press 2026

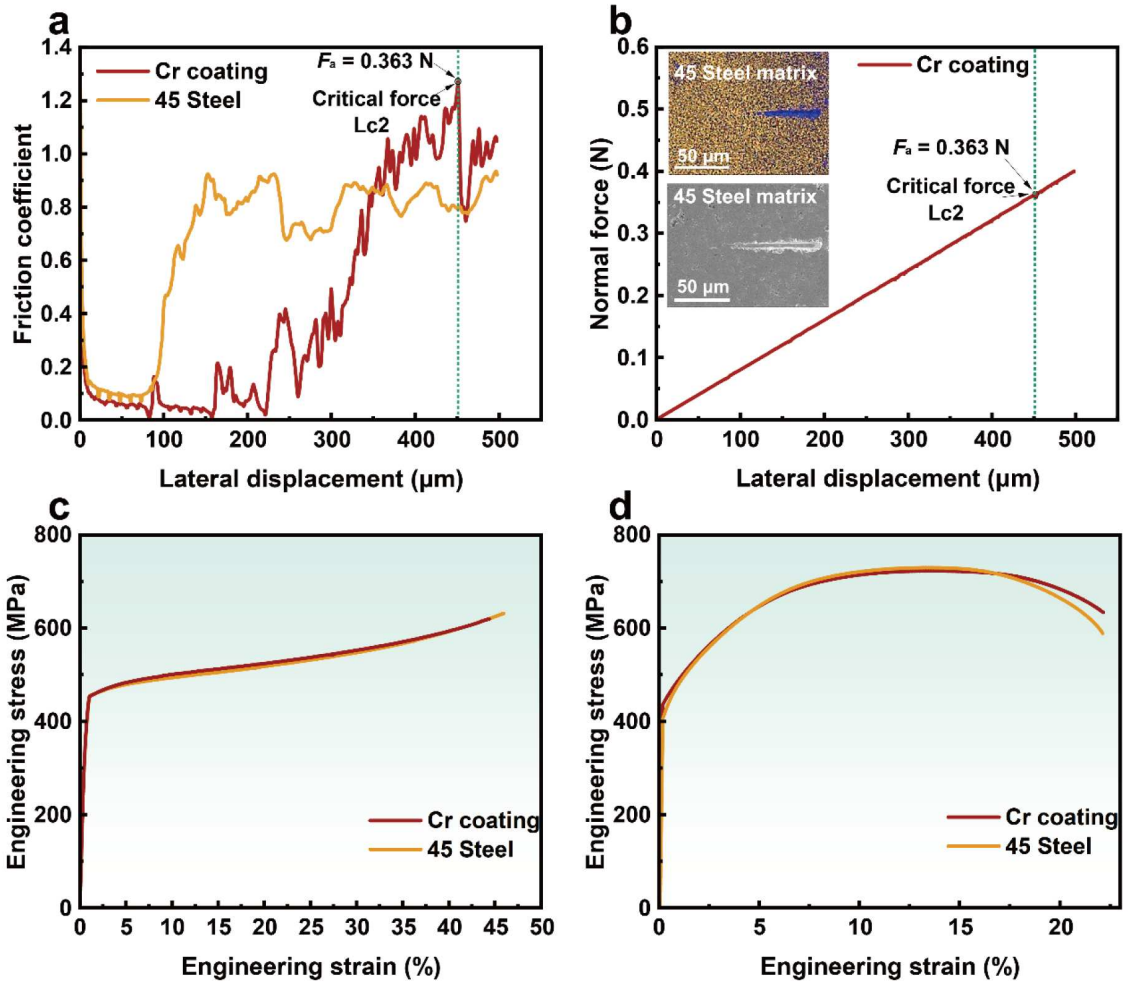

Figure 5 (a) Coefficient of friction versus lateral displacement for the Cr coating on 45 steel substrate. (b) Normal force versus lateral displacement for the Cr coating. The insets are SEM-EDS maps of the scratched surface; yellow and blue denote Cr and Fe, respectively. (c) Compression engineering strain-stress curves of 45 steel and the coated sample. (d) Tensile engineering strain-stress curves of 45 steel and the coated sample.

coating damage (300 μm) to complete delamination (450 μm).

$$\frac{1}{E} = \frac{1-\nu_{\text{sub}}^2}{E_{\text{sub}}} + \frac{1-\nu_{\text{tip}}^2}{E_{\text{tip}}}, \tag{1}$$

where ν_{sub} and ν_{tip} are the Poisson's ratio; E_{sub} and E_{tip} are the moduli of the substrate (45 steel) and diamond tip, respectively. Specifically, the 45 steel substrate has a modulus of 210 GPa and a Poisson's ratio of 0.26, while the diamond tip exhibits a modulus of 1140 GPa and a Poisson's ratio of 0.07.

$$P_0 = \left(\frac{FE}{\pi r}\right)^{1/2}, \tag{2}$$

where F is the load, r is the radius of the diamond tip, and E is the weighted E-modulus for the substrate material and diamond tip. Hertz contact requires elastic deformation, while plastic deformation dominates scratch contact of the coating in this study, and this causes systematic deviation in Hertz-calculated stress. This deficiency is common in scratch-Hertz combined calculation, because the elastic model cannot reflect changes in contact area and stress induced by plasticity. Nevertheless, the contact area deviation under elastoplastic conditions does not introduce an order-of-magnitude error into the Hertz-calculated stress, as the stress depends only weakly on the contact area through a fractional exponent. The calculation method is unified and standardized, so this nominal stress has the reference significance, and it can still characterize the mechanical features of the coating and the critical state of elastic-plastic transition [58].

Fig. 5c demonstrates high consistency between the compressive stress-strain curves of the coated sample and as-received 45 steel. During the elastic deformation stage, both specimens exhibit linear stress-strain relationships with nearly identical slopes (elastic modulus), confirming that the UVAMC process preserves the material's elastic properties. In the plastic deformation regime, synchronized stress evolution, comparable peak stresses (~600 MPa), and consistent strain hardening behavior verify that the coating process maintains the material's plastic deformation capability and compressive strength. The results of the tensile tests in Fig. 5d corroborate these findings, showing similarity in yield strength and strain hardening rate between coated and uncoated samples evidence that the ultrasonic treatment preserves the dislocation motion of the substrate. Also, the nearly superimposed ultimate tensile strength and the fracture elongation curves demonstrate that the UVAMC neither compromises fracture resistance nor deteriorates material ductility. This dual verification through compressive and tensile testing conclusively establishes that UVAMC enhances corro-

© Science China Press 2026

sion resistance while basically retaining the 45 steel substrate's critical mechanical properties, including elastic modulus, yield strength, tensile strength, and plastic deformation capacity. The tensile and compressive curves of coated and bare samples show little difference. This phenomenon is mainly attributed to the ultra-thin Cr coating (~13 μm), which exerts limited influence on the macroscopic mechanical properties of the sample. It is proven that UVAMC induces no significant microstructural alterations in the substrate material.

Modification validation, multi-material validation, and targeted coating of UVAMC

UVAMC technology demonstrates significant technical advantages in the deposition of Cr coatings, particularly in corrosion protection applications on metallic substrates such as 45 steel. As shown in Fig. 6a, the preliminary 48 h immersion results verify

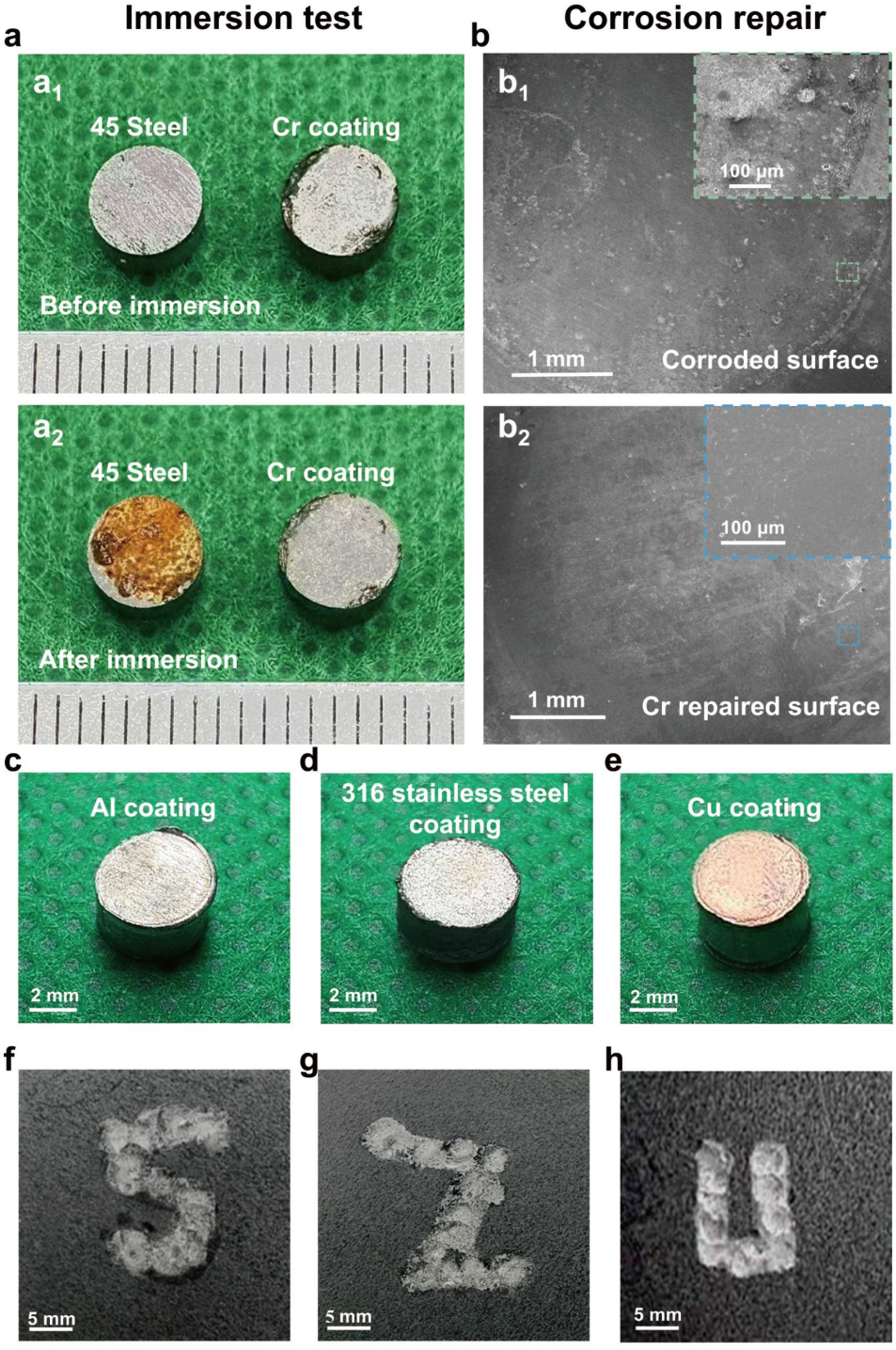

Figure 6 (a) Surface morphologies of samples: (a_1) before and (a_2) after immersion in 3.5 wt% NaCl solution for 48 h. (b) SEM images of the sample surface before and after corrosion repair: (b_1) before and (b_2) after repair. (c–e) Al, 316 stainless steel, and Cu coatings deposited on 45 steel surfaces. (f–h) Patterns "S", "Z", and "U" deposited on 45 steel.

© Science China Press 2026

that the Cr coating remains structurally intact without obvious damage after soaking in 3.5 wt% NaCl solution. To further evaluate long-period anticorrosion performance, extended immersion tests lasting 1 day, 5 days, and 13 days were supplemented, with corresponding macroscopic appearances and SEM micrographs provided in Fig. S4. For 45 steel, discrete microscale corrosion pits can be detected on the surface after 1 day of immersion. At the immersion duration of 5 days, visible rust regions form on the macroscopic surface, accompanied by extensive corrosion layers and rugged corroded microstructures under SEM observation. After 13 days of immersion, the entire surface of 45 steel suffers intensive uniform corrosion, and abundant corrosion features are homogeneously distributed throughout the inspected area. In contrast, the Cr-coated sample maintains an intact and smooth surface without obvious rust macroscopically within 5 days of immersion; only sporadic tiny corrosion pits start to form on the coating surface after 13 days of immersion. According to the 13-day test results, the Cr-coated sample shows better corrosion resistance than 45 steel. Furthermore, the coating system possesses self-healing capability: as illustrated in Fig. 6b, localized corrosion damage can be efficiently repaired via ultrasonic-assisted redeposition, restoring its protective performance. This feature significantly extends the service life of coated components and substantially reduces maintenance costs. Notably, UVAMC technology exhibits outstanding material adaptability. As shown in Fig. 6c–e, this technique is not only suitable for Cr powders but also successfully applicable to the high-quality coating preparation of various metal powders such as aluminum (Fig. 6c), 316 stainless steel (Fig. 6d), and copper (Fig. 6e). Fig. 6f–h display the S-, Z-, and U-shaped coatings prepared on 45 steel substrates via UVAMC, directly verifying the targeted coating capability of this technique. The coatings feature well-defined geometries without material overflow in the non-coated regions, demonstrating precise spatial control over deposition, which facilitates selective surface modification of specific regions on structural steel components.

UVAMC technology demonstrates advantages in surface coating for metallic substrates such as 45 steel: it produces dense, well-adhered Cr coatings with excellent corrosion resistance, features a unique self-healing capability to restore protective performance, exhibits broad material adaptability for various metal powders, and achieves precise targeted coating for selective surface modification, making it a highly promising technology for engineering surface modification.

CONCLUSIONS

This study demonstrates that UVAMC employs a unique low-temperature deposition mechanism. Based on this mechanism, UVAMC overcomes the shortcomings of conventional surface coating technologies, exhibiting significant improvements in both material adaptability and interfacial bonding stability. The Cr coating exhibits superior properties: a nanoscale elemental interdiffusion transition layer formed at the interface, providing reliable connections that yield a bonding strength of 66.0 MPa; the Cr coating shows not only improved corrosion resistance in aggressive environments, but also retains the substrate's original mechanical properties, including compressive and tensile strength. Furthermore, the successful coating of copper, aluminum, 316 stainless steel powders, and complex shape "SZU" demonstrates exceptional process adaptability and operational flexibility. These findings confirm that UVAMC provides an innovative solution for surface functionalization of metallic materials, combining efficient deposition characteristics with broad application versatility.

Received 17 June 2026; accepted 14 August 2026; published online 8 September 2026

1 Li Y, Tian Y, De Liu Y, *et al.* Titanium-steel composite plate with hot-rolled microstructures and its enhanced corrosion resistance in marine environment. Corrosion Sci, 2026, 259: 113469
2 Duan J, Wang M, Huang R, *et al.* A novel high-entropy alloy with an exceptional combination of soft magnetic properties and corrosion resistance. Sci China Mater, 2023, 66: 772–779
3 Wei XX, Zhang B, Wu B, *et al.* Enhanced corrosion resistance by engineering crystallography on metals. Nat Commun, 2022, 13: 726
4 Zhang B, Wang J, Wu B, *et al.* Unmasking chloride attack on the passive film of metals. Nat Commun, 2018, 9: 2559
5 Lv H, Chen P, Li MX, *et al.* Synergistic enhancement of corrosion resistance and strength through Ce-modified second phases in Mg-Mn-Zn alloys. Corrosion Sci, 2026, 264: 113745
6 Zhang B, Cui J, Wang F, *et al.* Evolution of the early-stage corrosion behavior of 2% Ni low-alloy steel in simulated marine atmosphere: regulation by low chromium content. Corrosion Sci, 2026, 262: 113685
7 Hussain Z, Wang X, Riaz I, *et al.* Experimental and multi-scale simulation evaluation of nanoclay/nanosilica epoxy coatings for enhanced corrosion protection of structural steel. Corrosion Sci, 2026, 260: 113574
8 Deng R, Peng Y, Meng Q, *et al.* Enhancing control over the degradation behavior of zinc alloy via MOF coating. Sci China Mater, 2024, 67: 4074–4086
9 Zhou C, Sun Y, Huang P, *et al.* Mussel cuticle granule-inspired nanocomposite coating derived from metal-organic frameworks for intelligent corrosion control. Sci China Mater, 2025, 68: 4238–4252
10 Dong L, Wei XW, Liu MJ, *et al.* Boosting corrosion resistance of environmental barrier coatings through surface aluminum modification against molten salts. Corrosion Sci, 2025, 244: 112646
11 Ran G, Xu W, Song T, *et al.* Comprehensive enhancement of pitting corrosion resistance in 2205 duplex stainless steel: mechanisms via defect-rich surface regulation. Corrosion Sci, 2026, 259: 113477
12 Xie C, Han J, Hou Y, *et al.* The spontaneous passivation of multi-principal element alloys III: influence of 5 at% elemental additions in the CoCrFeNi family. Corrosion Sci, 2026, 263: 113712
13 Bharati, Engelberg D, Unluer C. Characterisation of passive layer on steel immersed in MgO-SiO_2 binder suspension solution. Corrosion Sci, 2025, 255: 113149
14 Xu T, Yu L, Hu JM. *In-situ* Zn–Al layered double hydroxide conversion coatings prepared on galvanized steels by a two-step electrochemical method. Corrosion Sci, 2024, 233: 112057
15 Bai Q, Zhang L, Ke L, *et al.* The effects of surface chemical treatment on the corrosion behavior of an Al-B_4C metal matrix composite in boric acid solutions at different temperatures. Corrosion Sci, 2020, 164: 108356
16 Wang Q, Kainuma S, Yang H, *et al.* Durability and corrosion resistance of defective Zn- and Al-based thermal spray coatings on carbon steel plates in high-chloride environments. Results Eng, 2025, 28: 108206
17 Liu Y, Yang M, Tang J, *et al.* Anticorrosion performance of thermal spray coatings on corroded steel after surface preparation. Surf Coatings Tech, 2026, 520: 133039
18 Grinon-Echaniz R, Refait P, Jeannin M, *et al.* Study of cathodic reactions in defects of thermal spray aluminium coatings on steel in artificial seawater. Corrosion Sci, 2021, 187: 109514
19 Zheng L, Giallonardo JD, Behazin M, *et al.* Microstructure and initial corrosion response of electrodeposited/cold sprayed copper coating interface regions on used nuclear fuel containers. Corrosion Sci, 2025, 255: 113103
20 Liu W, Wang P, Shi W, *et al.* Achieving ultrafine grain strengthening

© Science China Press 2026

Cf/SiC-GH3536 joints brazed with Cu-Ti-WC composite interlayer via cold spray additive manufacturing. Additive Manufacturing, 2024, 89: 104258
21 Weinstein M, Falconer C, Doniger W, *et al.* Environmental degradation of electroplated nickel and copper coated SS316H in molten FLiNaK salt. Corrosion Sci, 2021, 191: 109735
22 He Z, Wu Z, Gao Z, *et al.* Erosion-corrosion behavior of Ni-Al-Cu coating on nickel-aluminium bronze alloy in 3.5 wt% NaCl solution. Corrosion Sci, 2024, 238: 112380
23 León J, Ter-Ovanessian B, Normand B, *et al.* Corrosion resistance of electroplated coatings based on chromium trivalent-baths. Surf Coatings Tech, 2024, 481: 130616
24 Zeng J, Shao J, Liu Y, *et al.* Enhancing hot corrosion resistance of NiCrAlYSi coatings by Al–Cr surface modification via chemical vapor deposition (CVD). Surf Coatings Tech, 2026, 526: 133361
25 Hudak OE, Scheiber A, Kutrowatz P, *et al.* High-temperature hot corrosion kinetics of PVD $Ti_{1-x}Al_xN$ coatings on Nimonic c-263. Corrosion Sci, 2024, 236: 112248
26 Zhao Y, Shen Z, Dong Z, *et al.* Grain boundary-controlled dissolution of Cr coatings on Zr alloy cladding in oxygenated high-temperature water. Corrosion Sci, 2026, 260: 113571
27 Xie XM, Zhao HL, Zhu JP, *et al.* Laser cladding $Ni_3Si/CrNi_3$ reinforced metal matrix composite coatings: microstructure evolution, tribological behavior and oxidation resistance. Surf Coatings Tech, 2025, 498: 131840
28 Dou K, Ge Y, Xue L, *et al.* Enhanced corrosion resistance in CoCrNi-CrC coating with micro-/nano-scale core-shell structure by tailoring laser cladding speed. Surf Coatings Tech, 2026, 526: 133322
29 Chen M, Yang K, Wang Z, *et al.* Corrosion performance of NV E690 steel and 316L stainless steel coating fabricated by underwater direct metal deposition. Corrosion Sci, 2023, 219: 111232
30 Poza P, Garrido-Maneiro MÁ. Cold-sprayed coatings: microstructure, mechanical properties, and wear behaviour. Prog Mater Sci, 2022, 123: 100839
31 Yin S, Fan N, Huang C, *et al.* Towards high-strength cold spray additive manufactured metals: methods, mechanisms, and properties. J Mater Sci Tech, 2024, 170: 47–64
32 Gugua EC, Ujah CO, Asadu CO, *et al.* Electroplating in the modern era, improvements and challenges: a review. Hybrid Adv, 2024, 7: 100286
33 Zheng J, Bock DC, Tang T, *et al.* Regulating electrodeposition morphology in high-capacity aluminium and zinc battery anodes using interfacial metal-substrate bonding. Nat Energy, 2021, 6: 398–406
34 Schalk N, Tkadletz M, Mitterer C. Hard coatings for cutting applications: physical vs. chemical vapor deposition and future challenges for the coatings community. Surf Coatings Tech, 2022, 429: 127949
35 Wang C, Zhang X, Lu Y, *et al.* Tailoring long-life, wear and corrosion resistant a-C: H coating for marine applications by PVD combined HC-PECVD co-deposition technology. Surf Coatings Tech, 2025, 513: 132450
36 Ma J, Yang C, Liu X, *et al.* Fast surface dynamics enabled cold joining of metallic glasses. Sci Adv, 2019, 5: eaax7256
37 Li L, Li X, Huang Z, *et al.* Joining of metallic glasses in liquid via ultrasonic vibrations. Nat Commun, 2023, 14: 6305
38 Liang X, Wu K, Fu J, *et al.* Fabrication of amorphous and high-entropy biphasic composites using high-frequency ultrasonic vibration. J Non-Crystalline Solids, 2022, 582: 121458
39 Wang J, Liu S, Huang P, *et al.* Ultrasonic powder consolidation of metallic glass/Al-6061 composites. Intermetallics, 2024, 174: 108462
40 Wu B, Cao B, Yu X, *et al.* Ultrasonic vibration enabled cold manufacturing of high thermal conductive Cu/diamond composites. Sci China Mater, 2026, 69: 2188–2200
41 Gomes I, Carneiro V, Outeiro J, *et al.* Unlocking the potential of ultrasonic consolidation: a critical review of process modelling and simulation frameworks. Int J Adv Manuf Technol, 2026, 144: 1581–1604
42 Li X, Fu J, Sun J, *et al.* Ultrasonic welding of metallic glasses: a review. Sci China Mater, 2025, 68: 2215–2229
43 Cheng Y, Sun Y, Zhang S, *et al.* Corrosion and wear resistance of inconel 625 and inconel 718 laser claddings on 45 steel. J Alloys Compd, 2025, 1013: 178368
44 Eich SM, Beinke D, Schmitz G. Embedded-atom potential for an accurate thermodynamic description of the iron-chromium system. Comput Mater Sci, 2015, 104: 185–192
45 Liu Z, Wang H, Haché MJR, *et al.* Prediction of heterogeneous microstructural evolution in cold sprayed copper coatings using local Zener-Hollomon parameter and strain. Acta Mater, 2020, 193: 191–201
46 Liu Z, Wang H, Haché M, *et al.* Formation of refined grains below 10 nm in size and nanoscale interlocking in the particle-particle interfacial regions of cold sprayed pure aluminum. Scripta Mater, 2020, 177: 96–100
47 Hassanzadeh-Tabrizi SA. Precise calculation of crystallite size of nanomaterials: a review. J Alloys Compd, 2023, 968: 171914
48 Varis T, Suhonen T, Calonius O, *et al.* Optimization of HVOF Cr_3C_2 NiCr coating for increased fatigue performance. Surf Coatings Tech, 2016, 305: 123–131
49 Gu B, Wang Y, Xu G, *et al.* Effect of ultrasonic impact on the microstructure and properties of 30%WC-Ni ceramic coatings by laser cladding. Ceramics Int, 2025, 51: 4677–4692
50 Zheng C, Chen R, Wang Q, *et al.* Great enhancement in corrosion resistance of Ti alloy by Mo element regulating β grain boundary and microstructure. Corrosion Sci, 2025, 256: 113237
51 Bahmani A, Moradi S, Lotfpour M, *et al.* Effect of grain size on the corrosion resistance of the $Fe_{41}Mn_{25}Ni_{24}Co_8Cr_2$ high entropy alloy. Corrosion Sci, 2024, 230: 111892
52 Wen X, Cui X, Liu Y, *et al.* A novel strategy for promoting corrosion and wear resistance of Mg–Li alloys: gradient eutectic high-entropy alloy coating induced by *in-situ* bidirectional diffusion. J Magnesium Alloys, 2025, 13: 2267–2282
53 Rong X, Li Y, Chen X, *et al.* Plain interface strategy toward the high corrosion performance of Al matrix composites. Sci China Mater, 2023, 66: 4295–4305
54 Ma K, Wang Y, Gu B, *et al.* Effect of ultrasonic vibration on the corrosion resistance of laser-cladded CrMnFeCoNi coatings. Mater Charact, 2026, 235: 116274
55 Gu B, Chu J, Wang Y, *et al.* Effects of ultrasonic impact treatment on the corrosion resistance of laser-cladded CrMnFeCoNi high-entropy alloy coatings. Surf Coatings Tech, 2024, 489: 131102
56 Ge Y, Cheng J, Ma L, *et al.* Tailoring microstructure and corrosion behavior of CoNiCrFeMoBSi high-entropy alloy coatings via Mo addition. Surf Coatings Tech, 2024, 489: 131129
57 Wu C, Ramaswamy Y, Gale D, *et al.* Novel sphene coatings on Ti-6Al-4V for orthopedic implants using sol-gel method. Acta BioMater, 2008, 4: 569–576
58 Kogut L, Etsion I. Elastic-plastic contact analysis of a sphere and a rigid flat. J Appl Mech, 2002, 69: 657–662

Acknowledgement The work was financially supported by the Key-Area Research and Development Program of Guangdong Province (2024B0101070001), the National Natural Science Foundation of China (52571191, 52401217, 52271150, and 52571190), and the Science, Technology and Innovation Commission of Shenzhen Municipality (RCJC20221008092730037, JCYJ20250604182240052, and JCYJ20240813141413018). We thank the Instrumental Analysis Center of Shenzhen University for the assistance with the electron microscope.

Author contributions Cao B conducted the investigation, formal analysis, validation, and data curation, designed the methodology, drafted the original manuscript, and reviewed and edited the manuscript. Wu B contributed to methodology and data curation. Bao W, Ruan W, and Liu X performed validation and data curation. Dong J, Pei C, Yin C, and Zhang D contributed to data curation. Zhang Y supervised the project, conducted formal analysis, and reviewed and edited the manuscript. Ma J took charge of investigation, formal analysis, validation, resources, project administration, funding acquisition and supervision, as well as manuscript review and editing.

Conflict of interest The authors declare that they have no conflict of interest.

© Science China Press 2026

Supplementary information Supplementary materials are available in the online version of the paper.

Bangliang Cao received his BSc degree from Guangdong University of Technology in 2024. Currently, he is a graduate student in the Jiang Ma Research Group at Shenzhen University. His research interests include ultrasonic vibration-assisted manufacturing.

Yu Zhang received his MA degree from Shenzhen University in 2022. He is currently a PhD student at the School of Materials Science and Engineering, Wuhan University of Technology. His research interests include metallic glass, high-entropy alloys, and ultrasonic vibration-assisted manufacturing.

Xiaodi Liu received his BEng degree in materials science and engineering from Shandong University in 2012 and his PhD degree from City University of Hong Kong in mechanical and biomedical engineering in 2018. He is currently an assistant professor at the College of Mechatronics and Control Engineering, Shenzhen University. His research interests include alloy design and mechanical behavior of metallic glasses.

Jiang Ma received his BSc degree in materials science and engineering from the Southeast University in 2009 and his PhD degree from the Institute of Physics, Chinese Academy of Sciences (CAS), Beijing, China, in 2014. He is currently a professor at the College of Mechatronics and Control Engineering, Shenzhen University, China, and received the Outstanding Teacher Award of Shenzhen in 2018. His research interests include the formation, functional application, and high-frequency dynamic loading behavior of metallic glasses.

超声振动辅助铬粉机械沉积于45钢表面以实现优异耐腐蚀性能

曹帮亮[1,2,3], 吴搏扬[1,2,3], 包文哲[1,2,3], 张宇[1,2,3,4*], 阮文清[1,2,3], 董杰[1,2,3], 裴超群[1,2,3], 尹存宏[5], 张大斌[5], 刘晓俤[1,2,3*], 马将[1,2,3*]

摘要 在金属基体表面制备功能涂层是提升金属材料防腐性能的有效手段. 但传统涂层制备工艺普遍耗时较长, 且大多依赖工件高温加热处理, 不可避免会产生热影响效应, 进而造成涂层致密度不足、界面结合强度偏低, 最终导致涂层在服役过程中发生大面积剥落失效. 为提升涂层的服役可靠性与制备效率, 亟需开发一种可在低温条件下快速成型、且能实现高界面结合强度的涂层制备方法. 本文提出一种超声振动辅助机械涂覆(UVAMC)工艺, 并在近室温环境下将铬粉成功沉积于45号钢基体表面. 该工艺仅需31 MPa低加工应力, 即可在1 s内制备出厚度可控(1.85、13.4、23.5 μm)、组织均匀致密的铬涂层. 涂层界面结合强度高达66.0 MPa, 该优异界面性能源于厚度约10–20 nm的原子尺度互扩散过渡层. 电化学测试结果表明, 在质量分数3.5%的氯化钠溶液中, 该铬涂层的腐蚀电流密度与304不锈钢接近, 具备优异耐蚀性能; 同时, 基体经涂覆处理后的抗压、抗拉强度均未发生衰减. 此外, 借助该UVAMC工艺, 本文还在45号钢表面完成铜粉、铝粉、316不锈钢粉末的沉积, 并制备出“SZU”图案化涂层. 上述研究结果证实, UVAMC工艺是一种高效、适用性广的制备技术, 可在金属基底上沉积各类功能粉体并针对性提升材料特定使用性能.

© Science China Press 2026